Journal of Applied Physics

RESEARCH ARTICLE | APRIL 15 2024

Design and fabrication of a sandwich detector for material discrimination and contrast cancellation in dual-energy based x-ray imaging

Rimcy Palakkappilly Alikunju ; Ian Buchanan ; Michela Esposito ; Jason Morehen ; Asmar Khan; Yiannis Stamatis; Nicolas Iacovou ; Edward Bullard ; Thalis Anaxagoras; James Brodrick ; Alessandro Olivo

J. Appl. Phys. 135, 154501 (2024)
https://doi.org/10.1063/5.0200269

Journal of Applied Physics ARTICLE pubs.aip.org/aip/jap

Design and fabrication of a sandwich detector for material discrimination and contrast cancellation in dual-energy based x-ray imaging

Cite as: J. Appl. Phys. **135**, 154501 (2024); doi: 10.1063/5.0200269
Submitted: 25 January 2024 · Accepted: 29 March 2024 ·
Published Online: 15 April 2024

Rimcy Palakkappilly Alikunju,[1] Ian Buchanan,[1] Michela Esposito,[1] Jason Morehen,[2] Asmar Khan,[2] Yiannis Stamatis,[2] Nicolas Iacovou,[2] Edward Bullard,[2] Thalis Anaxagoras,[2] James Brodrick,[2] and Alessandro Olivo[1,a)]

AFFILIATIONS

[1]Department of Medical Physics and Biomedical Engineering, UCL, Malet Place, London WC1E 6BT, United Kingdom
[2]ISDI Ltd, Highgate Business Centre, 33 Greenwood Place, London NW5 1LB, United Kingdom

[a)]**Author to whom correspondence should be addressed:** a.olivo@ucl.ac.uk

ABSTRACT

Dual-energy imaging represents a versatile and evolving technology with wide-ranging applications in medicine and beyond. Recent technological developments increased the potential for improved diagnostic accuracy and expanded imaging capabilities across various fields. The purpose of this work is to design and develop an energy-integrating multilayer detector, known as a sandwich detector, aimed at single-shot dual-energy imaging tasks such as material discrimination and contrast cancellation. The sandwich detector uses two complementary metal oxide semiconductor advanced pixel sensors of 50 μm pixel size. The top and bottom sensors detect low-energy (LE) and high-energy (HE) photons, with sensors coupled with 250 and 600 μm scintillators, respectively. For better spectral separation between layers without excessively affecting the detected statistic in the bottom layer, the insertion of a 0.25-mm Cu filter between the layers was found to be the optimal choice, from among the tested 0-, 0.25-, and 0.5-mm filter options. The thickness selection for scintillator and intermediate Cu filter was carried out through a dual-energy simulation model. The experiments confirmed the model's reliability in selecting the optimal thicknesses of the intermediate Cu filter, thereby providing reassurance also on the choice of the top scintillator.

I. INTRODUCTION

In conventional x-ray imaging, the information provided on the examined object is not sufficient to characterize it with sufficient precision for certain applications.[1] Dual-energy (DE) imaging, proposed by R. E. Alvarez and A. Macovski in 1976,[2] can provide significant improvements. It involves acquiring images at two distinct energy levels, typically a HE level and a low-energy (LE) level for enhanced material discrimination and improved image quality compared to conventional single-energy x-ray imaging. The technique exploits the differences in material attenuation characteristics at different energy levels allowing a degree of material identification and the detection of specific details against uneven, cluttered backgrounds. The potential applications of DE imaging include food inspection,[3] security applications,[4–7] chest imaging,[8–10] dual-energy cone beam computed tomography (DE CBCT) for radiotherapy,[11] breast imaging,[12,13] non-destructive testing (NDT),[1,14] and others.

Dual energy data acquisition can be performed by utilizing dual- or single-shot exposure techniques. In dual exposure, kVp switching can be used to acquire LE and high energy (HE) sequentially. This energy separation method works well for static items (e.g., off-line non-destructive testing) but is more time consuming and affected by motion artifacts when used for dynamic imaging or moving objects. Chest radiography, for example, shows blurriness near the heart due to cardiac activity. This limitation can be overcome by using single exposure techniques, implemented either by photon counters with energy resolving capabilities[15] or by making use of appropriate filters. The latter can provide access to large imaging areas in a cost-effective fashion, especially by using a detector with two receptor layers, separated by an intermediate

filter. The front detector records the low-energy photons and the back detector records the high-energy ones. Thus, two automatically registered images are acquired simultaneously, improving imaging speed and avoiding motion artifacts. However, if not optimized, this approach yields poor energy separation and excessive quantum noise.[1,16]

The primary goal of this study is to determine whether such an optimization can be implemented based on the current developments in complementary metal oxide semiconductor (CMOS) advanced pixel sensor (APS) technology. To accomplish this objective, a multi-layer energy integrating detector was constructed by stacking two CMOS APS sensors coupled with scintillators of appropriate thickness. A Cu filter was inserted between the two detectors to increase spectral separation; while the choice of Cu is somewhat arbitrary, a high Z material enables achieving a larger spectral separation with a lower filter thickness, and among these Cu is stable, non-toxic, cost-effective, and easy to source at reasonably high purity. The effectiveness of the "sandwich" detector is demonstrated by applying material discrimination and contrast cancellation techniques to real data; in this initial, exploratory study, this was limited to relatively low x-ray energies (RQA5 beam quality, i.e., 70 kV W spectrum with 21 mm of external Al filtration) and low Z target materials, with prospective applications in breast imaging and food inspection. While in this study the detector design was optimized for the above spectral characteristics, in general, the optimization process is an application-dependent task, the results of which would be different for a different x-ray spectral distribution.

II. MATERIALS AND METHODS

A. Development of the dual-energy algorithm model to design sandwich detector

Sections II A 1–II A 3 describe the design and development of the sandwich detector using a dual-energy algorithm model.

1. Sandwich detector model

The multilayer model was based on Beer Lambert's law given by Eq. (1), where transmission through each layer in the detector was mathematically modelled based on the incident x-ray intensity reaching it,

$$I = I_o e^{-\Sigma \mu x}, \quad (1)$$

where I is the transmitted intensity, I_o is the incident intensity, μ is the linear attenuation coefficient, and x is the thickness of each of the sandwich detector layers as shown in Fig 1. The model used RQA5 beam quality (70 kV, 21 mm external Al filtration) generated using Spektr 3.0 software.[17] The attenuation coefficient data were obtained from the NIST database.[18]

The simulation model ignores the carbon cover (1 mm—top and bottom) and the foam as the external 21 mm Al filtration hardens the beam to a degree where effects due to these become negligible.

The design specifications of the sandwich detector, mainly the top scintillator and Cu filter thicknesses, were determined by applying a dual-energy algorithm to the above-described sandwich detector model. The dual-energy algorithm model was based on the System Independent Rho-e/Z-e (SIRZ) method developed by Azevedo *et al.*,[19] which is mainly used for material classification by extracting the electron density (ρ_e) and effective atomic number (Z_e) of materials as explained in Sec. II A 2.

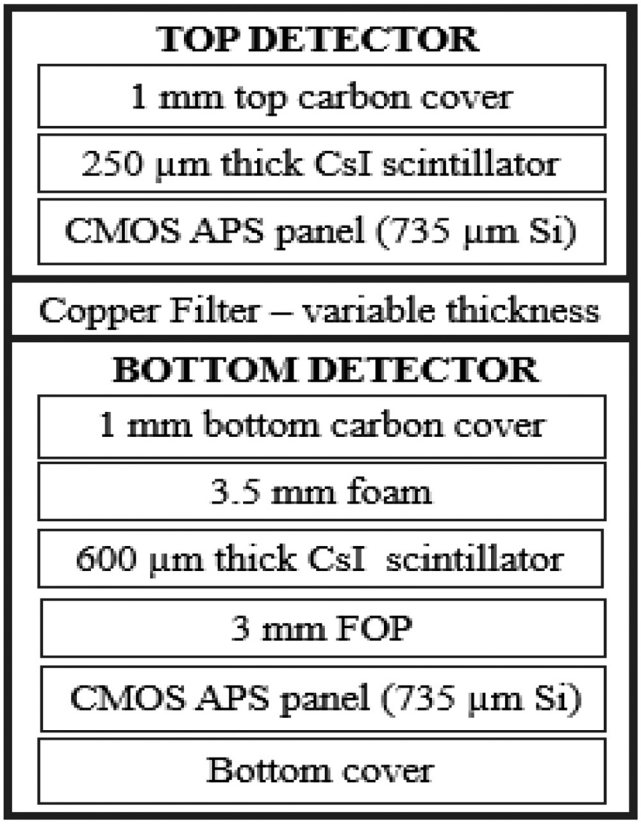

FIG. 1. Block diagram of the proposed sandwich detector.

2. Dual-energy algorithm model

The dual-energy algorithm model is based on the SIRZ method, itself based on the dual-energy decomposition technique proposed by Alvarez and Macovski in 1976.[2] According to Alvarez and Macovski, dual-energy attenuation data in the 30–200 keV energy range can be divided into two components, photoelectric absorption and Compton scatter, which describe the energy dependence of the x-ray attenuation coefficients as follows:

$$\mu(E) = (E^{-3})a_p + f_{KN}(E)a_c, \quad (2)$$

where E is the x-ray energy in keV, a_p and a_c are material-dependent photoelectric and Compton attenuation coefficients, and $f_{KN}(E)$ is the Klein–Nishina formula for free-electron Compton

scattering. The linear attenuation coefficient was obtained by

$$\mu(E) = -\log\left(\frac{T(E)}{t}\right), \tag{3}$$

where T(E) is the transmission image and t is the thickness of the phantom material(s) used.

By using $\mu(E_l)$, $\mu(E_h)$, $f_{KN}(E_l)$, and $f_{KN}(E_h)$ values from low- and high-energy measurements, a_p and a_c can be extracted by the matrix division as given by Eq. (4),

$$\begin{bmatrix} a_p \\ a_c \end{bmatrix} = \begin{bmatrix} E_l^{-3} & E_h^{-3} \\ f_{KN}(E_l) & f_{KN}(E_h) \end{bmatrix} \backslash \begin{bmatrix} \mu(E_l) \\ \mu(E_h) \end{bmatrix}. \tag{4}$$

The electron density ρ_e is directly proportional to a_c and is given by Eq. (5),

$$\rho_e = K_1 a_c, \tag{5}$$

where the coefficient K_1 is determined by calibration with reference materials.

The theoretical Z_e values were calculated for the reference materials; by using the a_p and a_c values derived from each of the reference materials, the unknown coefficients g and v indicated in Eq. (6) can be determined and used in the model,

$$Z_e = g\left(\frac{a_p}{a_c}\right)^{\frac{1}{v}}. \tag{6}$$

Once coefficients g, v, and K_1 are fixed by calibration, they can be used to extract the material characterization parameters ρ_e and Z_e of unknown materials by introducing them in the same Eqs. (4)–(6).

We used the following materials in this study: sodium chloride (NaCl), sodium (Na), sapphire (Al_2O_3), silica (SiO_2), boron (B), sodium bicarbonate ($NaHCO_3$), magnesium (Mg), aluminum (Al), silicon (Si), Plexiglas ($C_5O_2H_8$), and carbon (C). From the above materials, NaCl, Al, Si, and Plexiglas were chosen as unknown materials, i.e., their Z_e and ρ_e values were predicted by the calibrated dual-energy system model.

Dual-energy images (LE and HE) of dimensions 2000×200 pixels were simulated using the sandwich detector model to create the flat-field and phantom images of the reference and unknown materials, with Poisson noise added to all images assuming an incident flux of 23 000 photons/pixel. An averaged line profile ROI (1×10 pixels) extracted from these images was

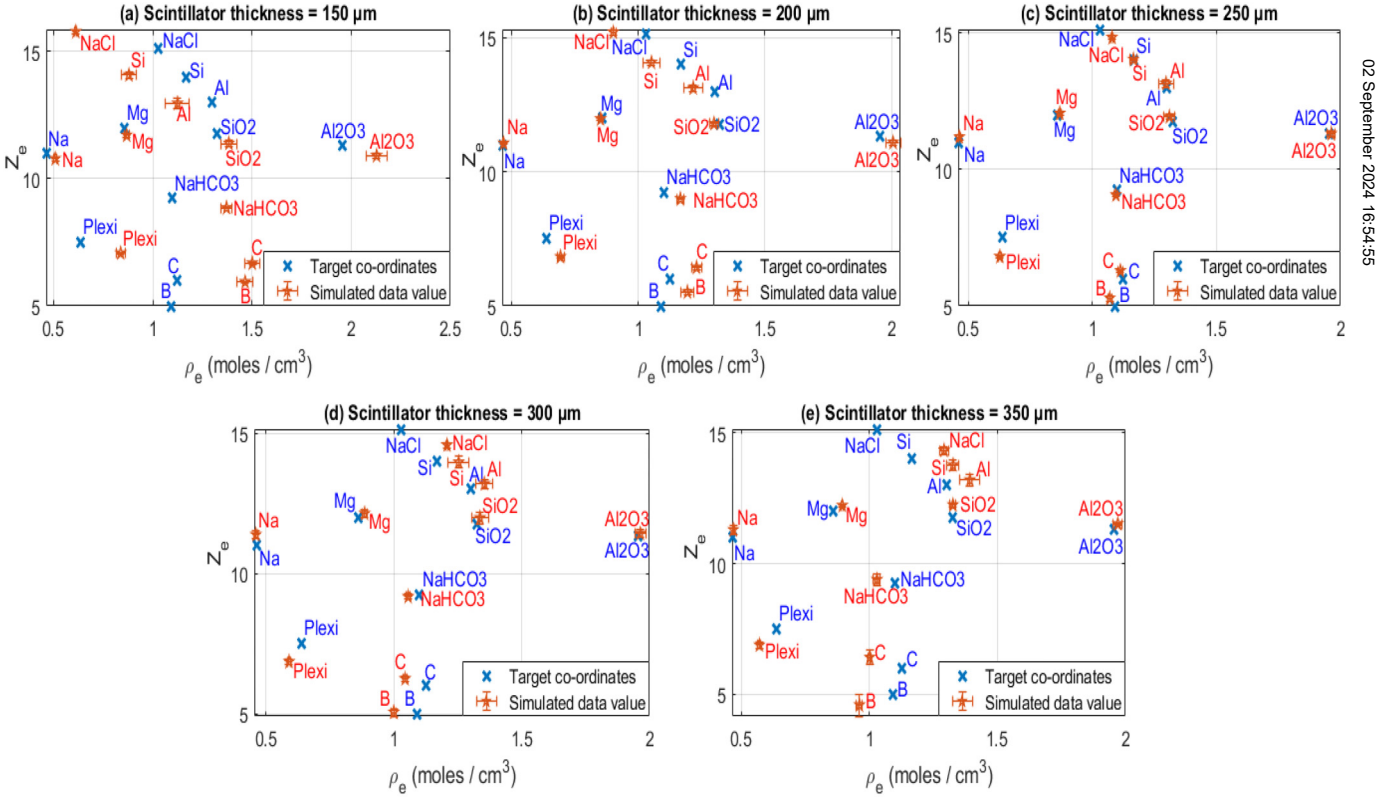

FIG. 2. Dual-energy algorithm for MD applied to calibration materials in the detector configuration with no intermediate filter with scintillator thicknesses of 150 (a), 200 (b), 250 (c), 300 (d), and 350 μm (e).

then fed to the dual-energy algorithm, which yielded a set of Z_e and ρ_e data for each calibration and unknown material as described above. The average value of Z_e or ρ_e and their respective standard deviation was recorded as $Z_e \pm \sigma_{Ze}$ and $\rho_e \pm \sigma_{\rho e}$. The dual-energy algorithm was applied separately to images created with the sandwich detector model with different top scintillator thicknesses ranging from 150 to 350 μm in 50 μm increments, and this entire procedure was repeated for each of the Cu filter thicknesses of 0, 0.25, and 0.5 mm. The values of the scintillator and filter thickness that led to an optimal ρ_e and Z_e in each case, as determined by the minimum chi square between extracted and theoretical values, were ultimately chosen.

As an example, simulated results for the no filter case showing material discrimination (MD) for scintillator thicknesses between 150 and 350 μm are shown in Fig. 2 and Fig. S1 in the supplementary material for reference (calibration) and unknown materials, respectively. Similar results were obtained using 0.25- and 0.5-mm filter thicknesses (not shown).

The χ^2 test results performed on the unknown materials for selecting the optimum scintillator thickness for all the filter cases are shown in Fig. 3.

Table I shows the top scintillator thicknesses that gave the best material characterization results (i.e., the lowest χ^2 value as per Fig. 3) in terms of Z_e and ρ_e for each of the Cu filters used. As can be seen, results are very consistent for ρ_e, less so for Z_e; however, once all values are simultaneously considered, a 250 μm thick scintillator seems to be the best option for the top detector. A 600 μm thick bottom scintillator (the thickest available for the actual detector construction) was considered to stop the maximum amount of high-energy photons.

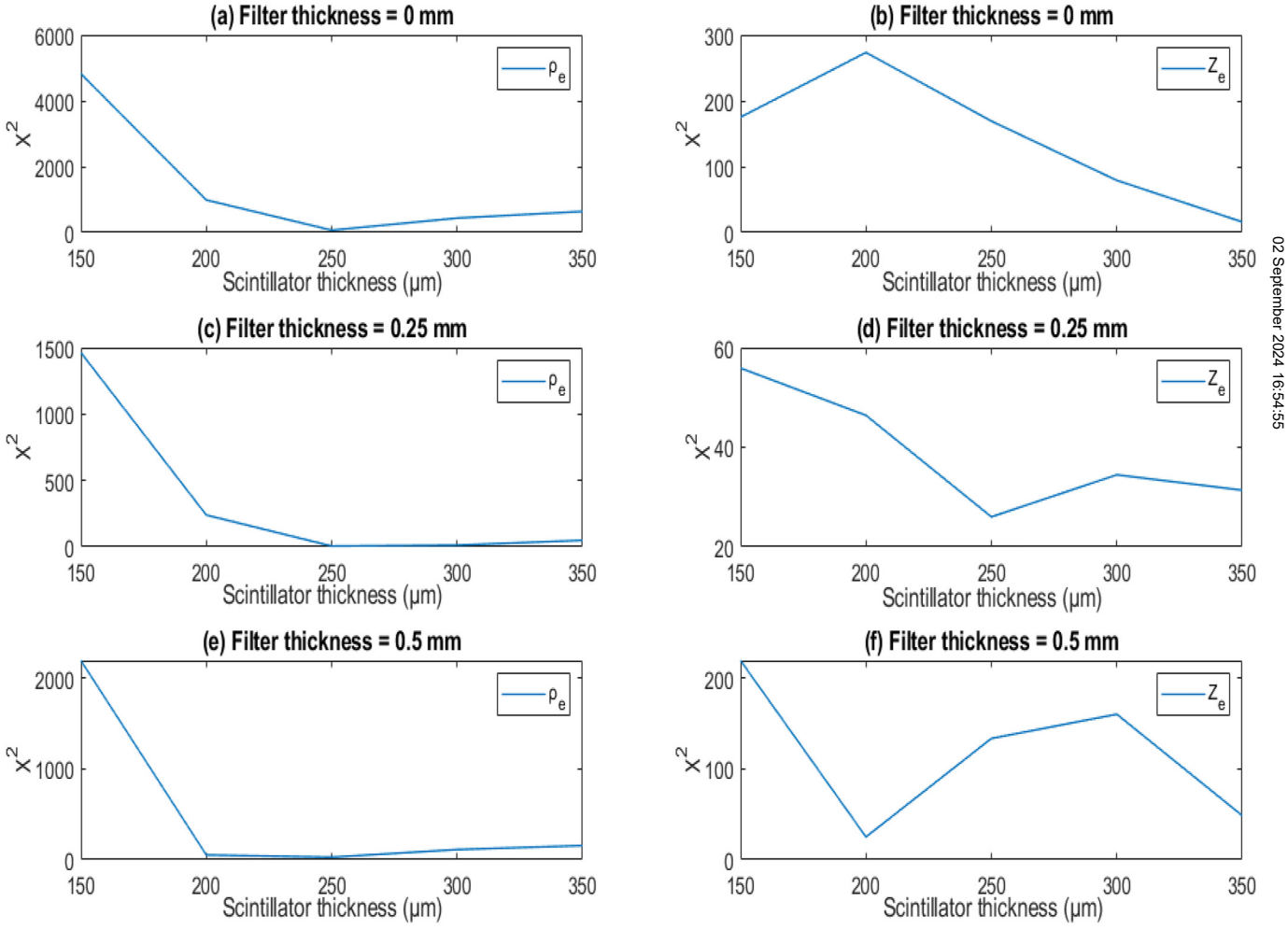

FIG. 3. χ^2 test applied to retrieved and targeted ρ_e and Z_e values for unknown materials for (a) and (b) 0 mm, (c) and (d) 0.25 mm, and (e) and (f) 0.5 mm Cu filter thickness to select the optimal top scintillator thickness in each case.

TABLE I. Top scintillator thicknesses resulting in the minimum χ^2 values for various thicknesses of the intermediate Cu filter.

Filter thickness (mm)	Electron density (ρ_e)	Effective atomic number (Z_e)
0	250	350
0.25	250	250
0.5	250	200
Average scintillator thickness (μm)	250	267

Table II shows the percentage of photons absorbed by different layers when using 0-, 0.25-, 0.5-, 0.75-, and 1-mm thick Cu intermediate filters. As can be seen, thick filters such as 0.75 and 1 mm reduce the number of photons reaching the bottom detector very significantly. Hence, in the following, we will only consider Cu thicknesses of 0-, 0.25-, and 0.5-mm as intermediate filters for the sandwich detector. For beam quality RQA5, these correspond to an average spectral energy of 50.4 keV in the top detector and of 55.3, 56.8, and 57.8 keV, respectively, in the bottom one. The optimum filter thickness among these three will be selected using the same χ^2 minimization test described above.

Figure 4 and Fig. S2 in the supplementary material present the material characterization results for calibration and unknown materials (respectively) by using Cu filter thicknesses of 0, 0.25, and 0.5 mm, with top and bottom scintillator thicknesses fixed at 250 and 600 μm, respectively.

Figure S3 in the supplementary material presents the results for the reduced χ^2 test to determine the optimum thickness for the intermediate Cu filter, with the obtained numerical values summarized in Table III.

All these results consistently show best performance for a 0.25-mm Cu filter. In summary, our design study indicates a 250 μm thick top scintillator with 0.25-mm thick intermediate Cu filter as the best choice for a sandwich detector configuration to be used with beam quality RQA5; these specifications were ultimately used in the development of the sandwich detector, as described in Sec. II A 3. While it was impossible to change the thickness of the top scintillator once this was installed, the detector design allowed experimenting with different intermediate filter thicknesses, results from which confirmed the model's prediction as discussed below.

3. Sandwich detector development

The sandwich detector schematic and a photo of the assembled prototype are shown in Fig 5. The top- and bottom-layer detectors were housed in aluminum frames with the top one being open at the bottom, i.e., with no aluminum in the path of the top sensor. The top detector uses a 250 μm thick flexible substrate scintillator (FSS) coupled with the CMOS APS sensor without a fiber optic plate (FOP). There is a 3 mm slot between the lower end of the top sensor and the carbon cover of the bottom one to accommodate the intermediate Cu filter. The bottom-layer detector uses a 600 μm CsI scintillator coupled to the CMOS APS sensor by a 3 mm FOP. The main objective of adding the FOP is to protect the bottom sensor from direct interaction of the high-energy x rays. Both top and bottom sensors have 50 μm pixel pitch (pp). A 3.5 mm foam layer was used to support the scintillator firmly on the sensor and the FOP in the bottom detector. The main design parameters of the sandwich detector are given in Table IV.

The sandwich detector was built at ISDI, an image sensor manufacturer in London, UK.[20] The detector was used for experimental validation of applications such as material characterization, i.e., finding the electron density (ρ_e) and effective atomic number (Z_e) of unknown materials and for contrast cancellation between materials, to allow the detection of specific details against an even background.

B. Material discrimination using dual-energy algorithm

For the purpose of material discrimination, the sandwich detector was calibrated separately by using experimentally collected data and by using simulated averaged line profiles of the phantom materials to predict the ρ_e and Z_e of unknown materials. The used reference and unknown materials were discussed in Sec. II E.

A cross-comparison of the experimental and simulated results was also done to validate the model-based mid filter selection described above. Results are presented in Sec. III A.

TABLE II. Percentage of photons absorbed by each layer at RQA5 beam quality.

	Cu filter thickness				
Sandwich detector layers	0 mm	0.25 mm	0.5 mm	0.75 mm	1 mm
Carbon cover—top (%)	4.2	4.2	4.2	4.2	4.2
CsI-top (%)	69.7	69.7	69.7	69.7	69.7
Si-Layer—top (%)	1.7	1.7	1.7	1.7	1.7
Cu filter (%)	0.0	9.2	14.5	17.8	19.9
Carbon cover—bottom (%)	1.0	0.6	0.4	0.3	0.2
Foam—bottom (%)	0.2	0.2	0.1	0.1	0
CsI—bottom (%)	21.1	13.1	8.4	5.6	3.7
Fiber optic glass plate (%)	0.5	0.3	0.2	0.2	0.1
Silicon—bottom (%)	0.1	0.1	0.0	0.0	0.0
Remaining photons from bottom Si (%)	1.5	1.0	0.7	0.5	0.4

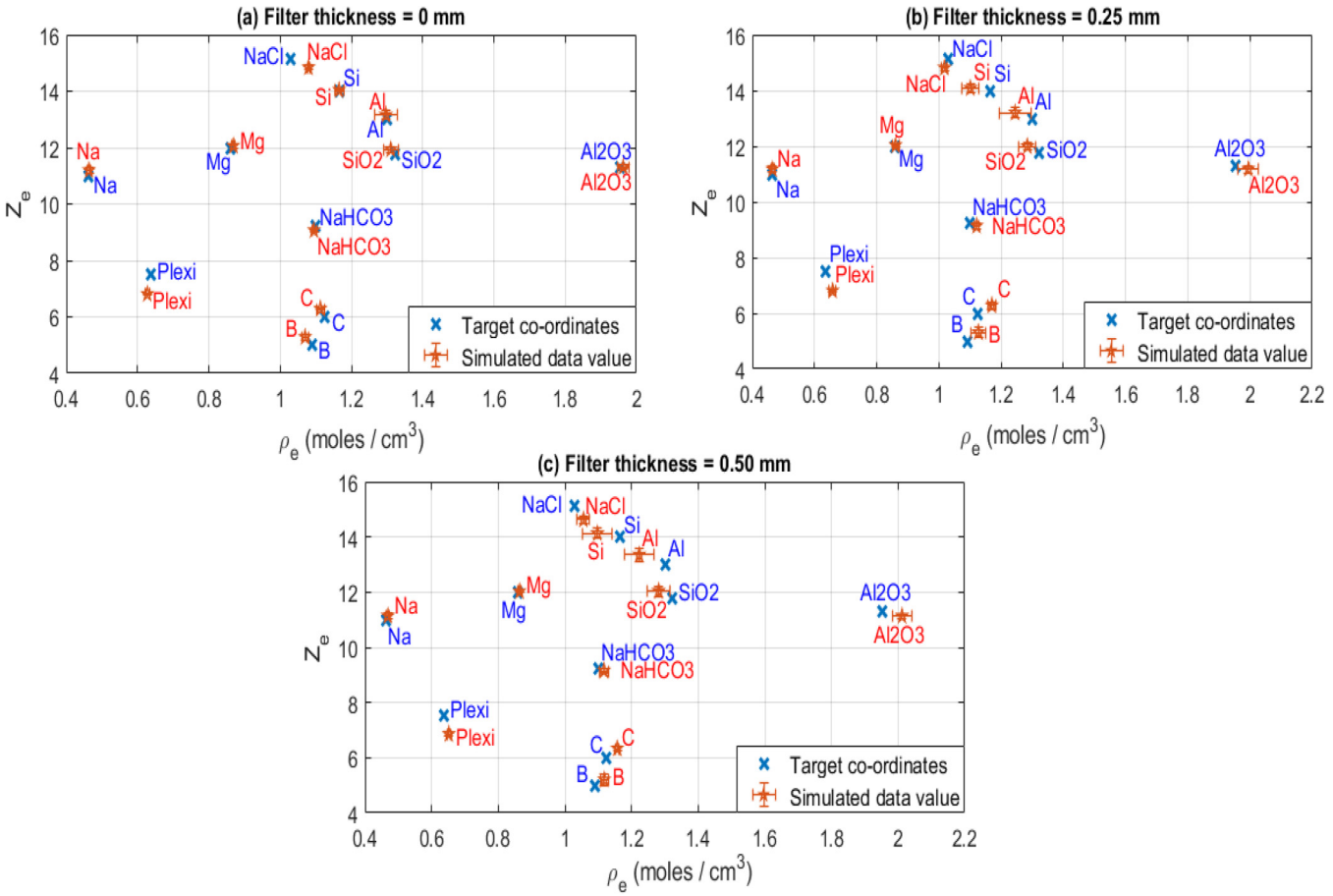

FIG. 4. Dual-energy algorithm for MD applied to calibration materials to select the optimum filter thickness for a fixed top and bottom scintillator thickness of 250 and 600 μm, respectively. The no filter case and filter thicknesses of 0.25 and 0.5 mm are shown in panels (a)–(c), respectively.

C. Dual-energy contrast cancellation technique

The dual-energy contrast cancellation technique, introduced by Alvarez and Macovski (1976) and further developed by Lehmann et al (1981), relies on the decomposition of the mass attenuation coefficient of a given material ξ into a linear combination of the mass attenuation coefficients of two base materials, α and β as given by Eq. (7),[2,21]

$$\frac{\mu_\xi(E)}{\rho_\xi} = a_1\left(\frac{\mu_\alpha(E)}{\rho_\alpha}\right) + a_2\left(\frac{\mu_\beta(E)}{\rho_\beta}\right), \tag{7}$$

where $\mu_\xi(E)$, $\mu_\alpha(E)$, and $\mu_\beta(E)$ and ρ_ξ, ρ_α, and ρ_β are the linear attenuation coefficients and densities of ξ, α, and β, respectively, E indicates the energy dependence, and a_1 and a_2 are coefficients related to the materials' densities and thicknesses.

Multiplying Eq. (7) by the thickness and density of material ξ allows expressing the logarithmic transmission M of the absorbing material in terms of the linear attenuation coefficients of base materials alpha and beta, resulting in Eq. (8),

$$M = \mu_\xi t_\xi = A_1\,\mu_\alpha(E) + A_2\mu_\beta(E), \tag{8}$$

where

$$A_1 = a_1 t_\xi\left(\frac{\rho_\xi}{\rho_\alpha}\right);\ A_2 = a_2 t_\xi\left(\frac{\rho_\xi}{\rho_\beta}\right). \tag{9}$$

TABLE III. χ^2 test summary to determine optimum filter thickness.

Filter thickness (mm)	Electron density (ρ_e)	Effective atomic number (Z_e)
0	69.8	169.2
0.25	5.7	26.0
0.5	27.1	133.5

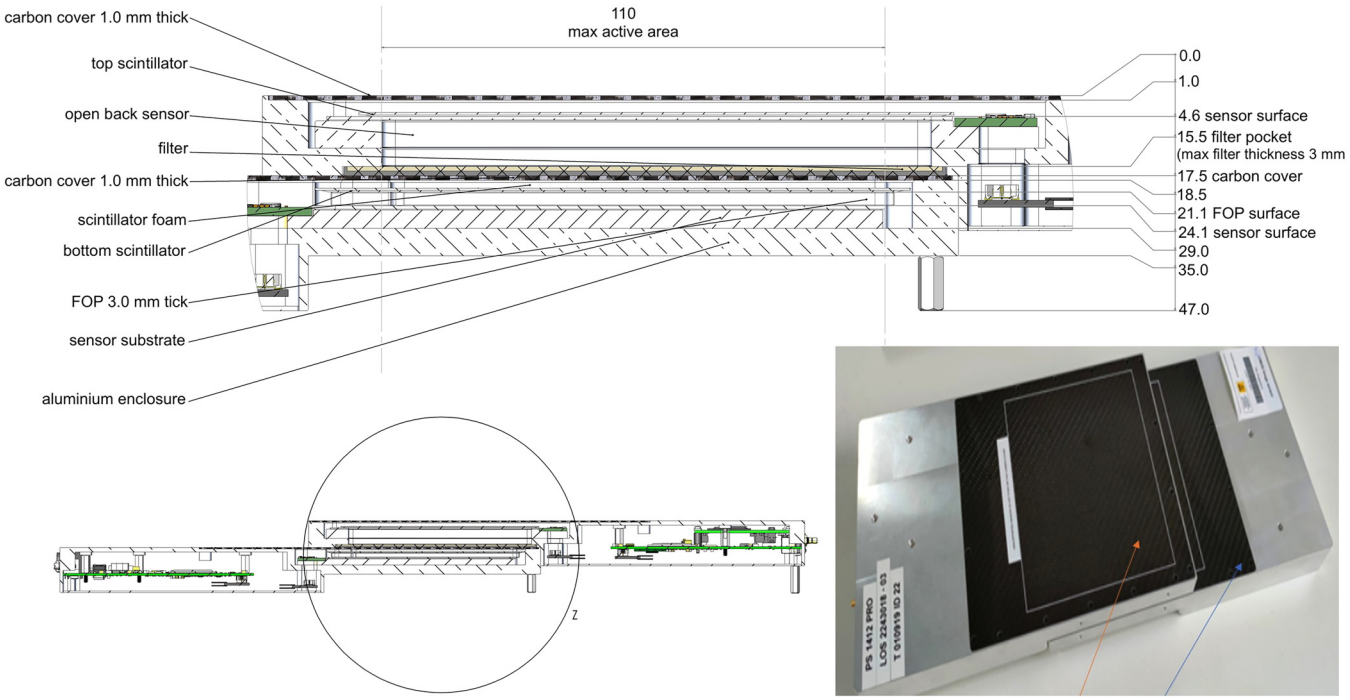

FIG. 5. Sandwich detector schematic and photo of the assembled prototype (bottom right inset); the orange and blue arrows in the latter point at the top and bottom detector layers, respectively.

By measuring the logarithmic transmission of the x-ray beam at two distinct energies, namely, LE and high energy (HE), the following systems of equations can be obtained:

$$M_l = A_1\,\mu_\alpha(E_l) + A_2\mu_\beta(E_l), \tag{10}$$

$$M_h = A_1\,\mu_\alpha(E_h) + A_2\mu_\beta(E_h), \tag{11}$$

where

$$M_l = \ln\left(\frac{I_{ol}}{I_l}\right) \text{ and } M_h = \ln\left(\frac{I_{oh}}{I_h}\right). \tag{12}$$

Here, the bi-dimensional matrices M_l and M_h represent the pixelwise logarithmic transmission, I_{0l} and I_{0h} are the initial intensities measured from the flat-field images, and I_l and I_h are the transmitted fluences measured from phantom images taken from the top and bottom sensors, respectively.

The solution of the system provides the coefficients A_1 and A_2 given by Eqs. (13) and (14),

$$A_1 = \frac{M_h\mu_\beta(E_l) - M_l\mu_\beta(E_h)}{\mu_\alpha(E_h)\mu_\beta(E_l) - \mu_\beta(E_h)\mu_\alpha(E_l)}, \tag{13}$$

$$A_2 = \frac{M_l\mu_{\beta\alpha}(E_h) - M_h\mu_\alpha(E_l)}{\mu_\alpha(E_h)\mu_\beta(E_l) - \mu_\beta(E_h)\mu_\alpha(E_l)}. \tag{14}$$

According to Lehmann *et al.*, M can be conveniently represented by a vector in a two-dimensional basis plane. The length of the logarithmic transmission vector is proportional to the thickness t_ξ of the material and is given by $L = \sqrt{(A_1^2 + A_2^2)}$; the characteristic angle of the material in the basis plane is given by $\theta = \tan^{-1}\frac{A_1}{A_2}$.

TABLE IV. Construction parameters for the sandwich detector.

Parameter	Specifications
Detector type	Dual-layer CMOS APS
Top detector panel (low-energy sensor)	2802 × 2400, 50 μm pp, coupled with 250 μm FSS
Middle layer filter for spectral separation	Cu filter slot to accommodate 0.25-, 0.5-, and 0.7-mm filters
Bottom detector panel (high energy sensor)	2802 × 2400, 50 μm pp, coupled with 600 μm CsI
Separation between sensor surfaces	19.5 mm
Data interface	GigE

If another material ψ is embedded in a volume of material ξ, the contrast between these two materials can be forced to vanish if the respective logarithmic transmission vectors, M_1 and M_2, are projected along a certain direction defined by the angle ϕ, thereby allowing for a prospective third material to be observed against a uniform background. ϕ is known as the contrast cancellation angle. The projection images at any projection angle φ are given by[22]

$$C = A_1 \cos\varphi + A_2 \sin\varphi = fM_h + gM_l, \tag{15}$$

where C is the basis projection image and A_1 and A_2 are given by Eqs. (13) and (14), both calculated on a pixel-by-pixel basis. M_l and M_h are logarithmic transmissions at low and high energy, respectively. f and g are given by

$$f = \frac{\mu_\beta(E_l)}{r}\cos\varphi - \frac{\mu_\alpha(E_l)}{r}\sin\varphi, \tag{16}$$

$$g = \frac{\mu_\alpha(E_h)}{r}\sin\varphi - \frac{\mu_\beta(E_h)}{r}\cos\varphi, \tag{17}$$

$$r = \mu_\alpha(E_h)\,\mu_\beta(E_l) - \mu_\beta(E_h)\mu_\alpha(E_l). \tag{18}$$

To calculate the contrast cancellation angle (ϕ) between two materials, say ξ and ψ, the difference in contrast between the two materials at ϕ has to be equated to zero,

$$\Delta C = 0, \text{ i.e., } C_\xi - C_\psi = 0. \tag{19}$$

Substituting the value of C in Eq. (19) results in Eq. (20),

$$\Delta C = f(M_{h\xi} - M_{h\psi}) + g(M_{l\xi} - M_{l\psi}) = 0. \tag{20}$$

Solving the above equation yields the contrast cancellation angle and is given by Eq. (21),

$$\phi = \tan^{-1}\left(\frac{\{\mu_\beta(E_l)^*(M_{h\xi} - M_{h\psi})\} + \{\mu_\beta(E_h)^*(M_{l\psi} - M_{l\xi})\}}{\{\mu_\alpha(E_l)^*(M_{h\xi} - M_{h\psi})\} + \{\mu_\alpha(E_h)^*(M_{l\psi} - M_{l\xi})\}}\right). \tag{21}$$

D. Experimental setup

The material characterization and contrast cancellation experiment were performed by using an x-ray source with a tungsten (W) anode placed inside a large x-ray cabinet operated at RQA5 beam quality (70 kV) as defined by IEC standards,[23] with 21 mm external Al filtration used throughout the measurements. The various phantoms described in Sec. II E were positioned on top of the detector. The experimental setup is as shown in Fig. 6.

E. Phantom materials

For material characterization, the reference materials used for calibration were Al, Si, Plexiglas, and NaCl, positioned for imaging as shown in Fig 7(a). The same materials were used as calibration and unknown materials. The discrimination results for calibration and

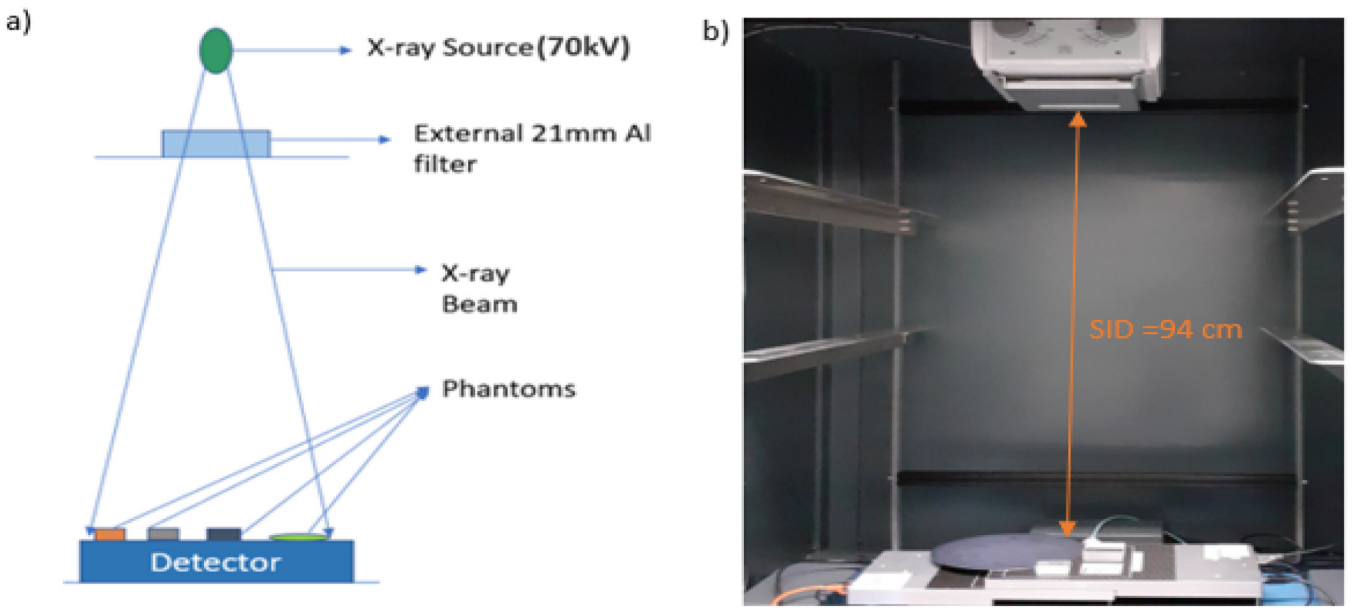

FIG. 6. (a) Schematic of the experimental setup; (b) photograph of the built sandwich detector (bottom) placed inside the x-ray cabinet.

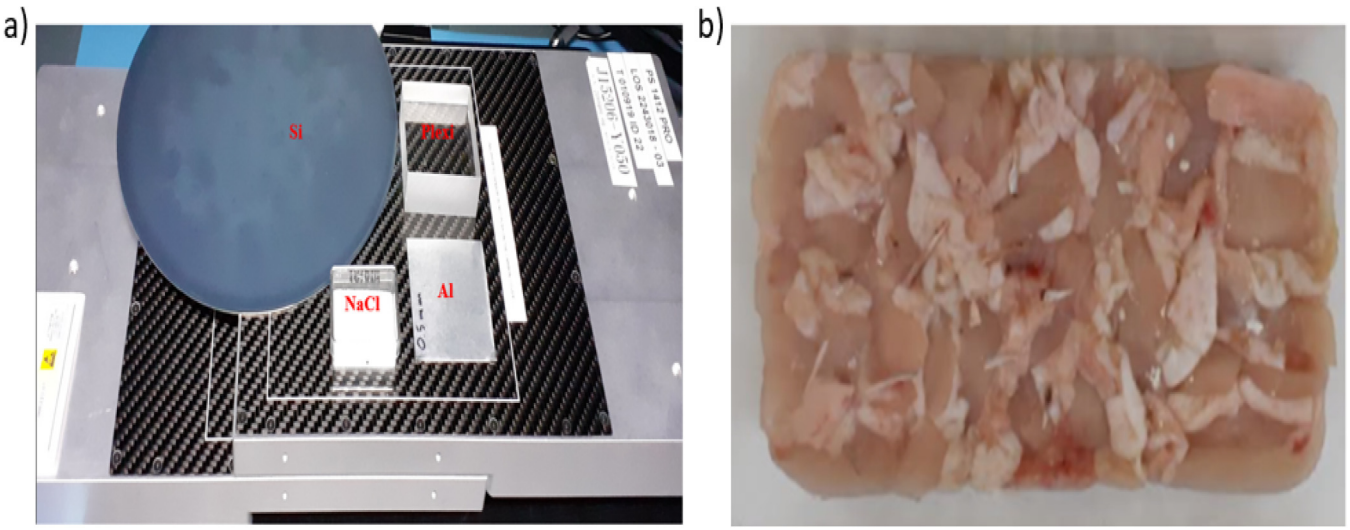

FIG. 7. (a) Material characterization phantoms and (b) lean and fat phantom.

unknown materials were obtained by making use of different, physically separated (and therefore independent) ROIs extracted from the images of each material. The constant parameters (g, ν, and k) fixed through calibration were then used to predict electron density (ρ_e) and effective atomic number (Z_e) of the unknown materials by using the dual-energy algorithm described in Sec. II A 2.

The phantom material used for the contrast cancellation experiment consists of chicken lean and fat tissue, on top of which some thin bones and calcium deposits were placed as "target" details as shown in Fig 7(b). Lean and fat were chosen as the base materials α and β, respectively. The attenuation coefficients of lean and fat were measured experimentally to extract the values of A_1 and A_2 as explained in Sec. II C to obtain the contrast basis images given by Eq. (15).

F. Signal-to-Noise Ratio (SNR) evaluation for contrast cancellation technique

The SNRs of bones and calcifications with respect to lean were evaluated at the contrast cancellation angles. The formula for SNR is given by

$$\mathrm{SNR} = (m_{bone,\ calcifications} - m_{BKGD})/\sigma_{BKGD}. \tag{22}$$

where $m_{bone,calcifications}$ is the mean intensity in an ROI taken from the area containing bones and calcifications and m_{BKGD} and σ_{BKGD} are mean intensity and standard deviation (respectively) extracted from ROIs taken in a background region (some specific examples are provided later in Fig. 11).

The SNR that satisfies the Rose criterion,[24] i.e., a minimum SNR of 5 for effective detail detection, was used as the criteria to determine the optimum filter to use in the sandwich detector configuration when the target application is contrast cancellation.

G. Image preparation procedure

Image preparation for material discrimination and contrast cancellation was done in the same way, except for the application of a median filter in the latter case. Both flat-field and phantom images were corrected for gain and offset. 60 images of the test phantoms were averaged to study the effectiveness of the dual-energy contrast cancellation algorithm. The gain map used for correcting the images used an average of 35 dark- and flat-field images. A correction factor was applied to phantom images according to the difference in intensity between corresponding flat-field and phantom images for top and bottom sensors, respectively. The transmission image (μt) was obtained by using the formula

$$\mu t = \log\left(\frac{I_{flat\_field}}{I_{phantom}}\right), \tag{23}$$

where $I_{flat\text{-}field}$ = flat-field image intensity and $I_{phantom}$ = phantom image intensity.

A slight mismatch was observed between top and bottom sensor images due to the small difference in magnification of the image in the bottom sensor compared to the top one. This was corrected by using the ImageJ plugin "Linear Stack alignment using SIFT."[25]

For the MD experiment, an ROI was selected from the MD μt phantom images and divided by the corresponding thicknesses to obtain the μ values. For the contrast cancellation experiment, a median filter was applied to the top and bottom sensor images, and the attenuation coefficients of the basis materials were measured by selecting a suitable ROI from the lean and fat regions of the phantom.

III. RESULTS AND DISCUSSION

A. Material discrimination results

The experiment was conducted while varying the intermediate filter thicknesses between the top and bottom detectors, namely, by using 0-, 0.25-, and 0.5 mm copper filters. The phantom materials are described in Sec. II E. Z_e and ρ_e data were extracted both experimentally and by using the simulation model for all the filter

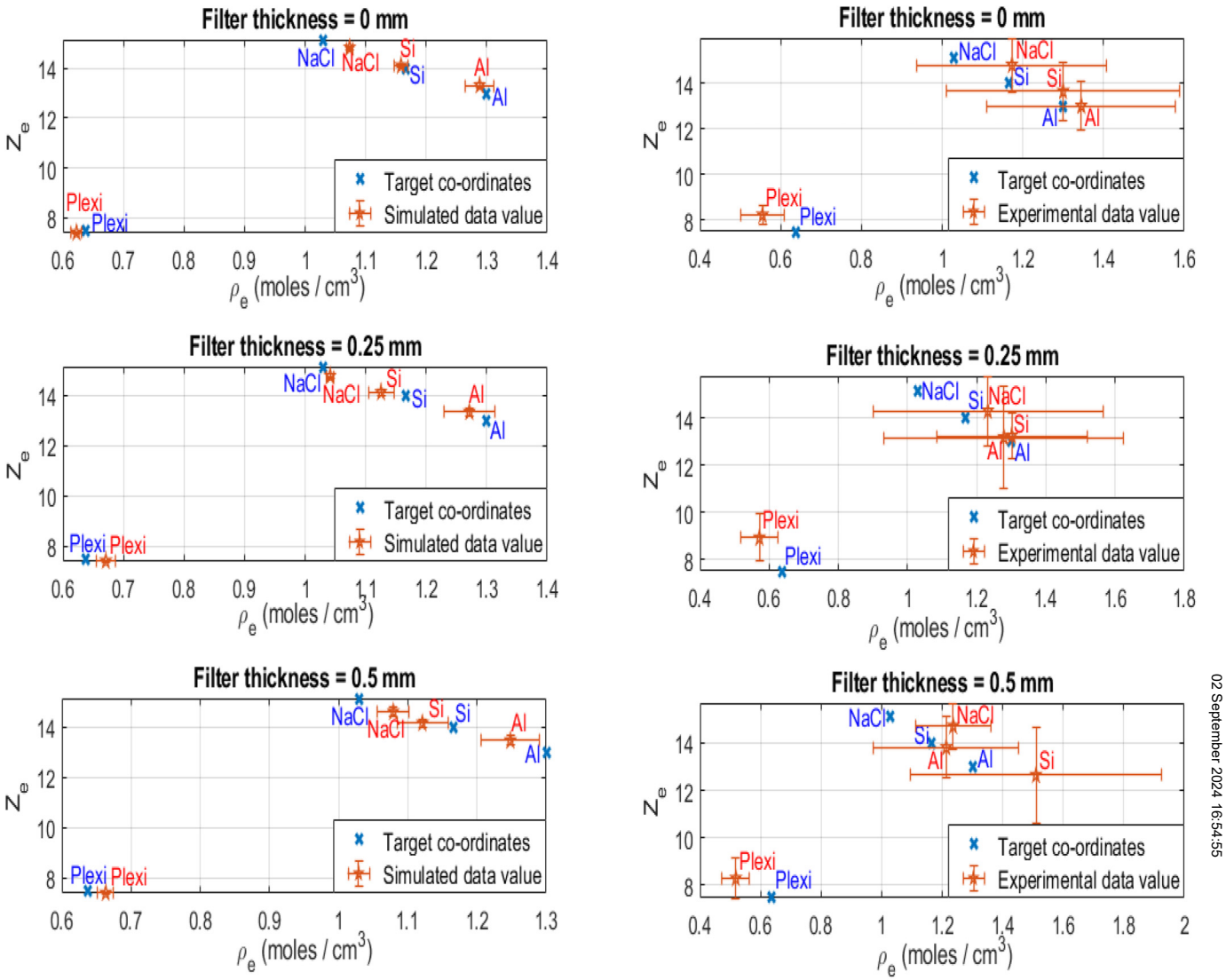

FIG. 8. Simulated (left column) and experimental (right column) results for calibration materials using 0 mm (top row), 0.25 mm (middle row), and 0.5 mm (bottom row) thick Cu filters.

configurations. The MD results for calibration materials are shown in Fig. 8, and the unknown materials are shown in Fig. S3 in the supplementary material. As can be seen, experimental results largely follow the trend observed in the simulated data, albeit with some increased degree of deviation from the target values and correspondingly larger error bars.

TABLE V. Unknown materials χ^2 test.

	Experiment		Simulation	
Filter thickness (mm)	ρ_e	Z_e	ρ_e	Z_e
0	78.92	4.77	219.77	6.34
0.25	5.06	10.43	7.47	2.65
0.5	72.60	34.79	39.35	94.53

A χ^2 test was performed on the simulation and experimental vs target Z_e and ρ_e values of the unknown materials to determine the filter thickness that gives the best results, with the outcome presented in Table V.

As can be seen, with a single exception (experimental Z_e), the 0.25-mm filter provides the best results, as was predicted by the model (see Sec. II A).

B. Contrast cancellation results

The aim of this part of the experiment was to visualize thin bones and calcifications against a uniform background, starting

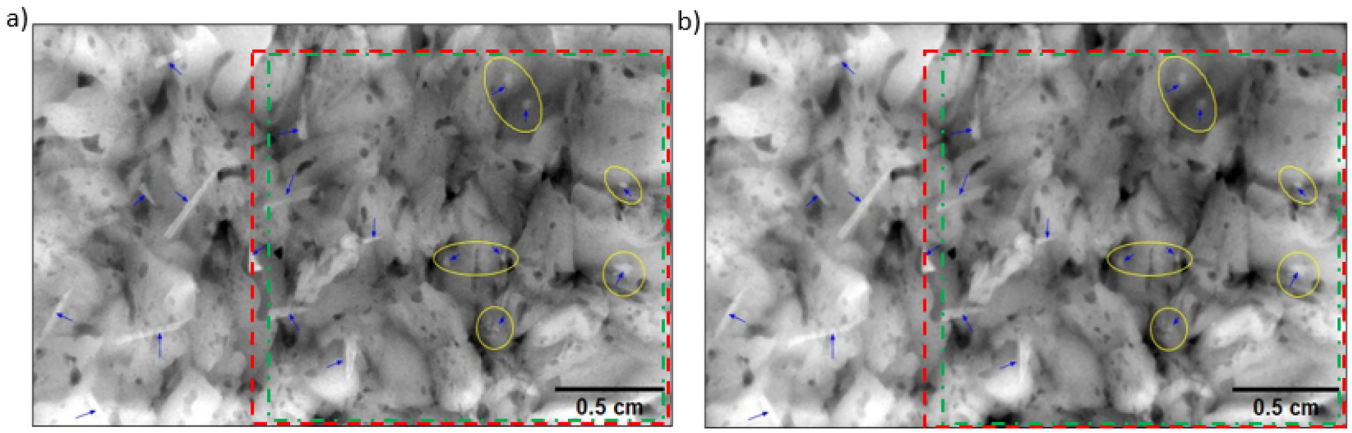

FIG. 9. (a) Top sensor (LE) and (b) bottom sensor (HE) logarithmic transmission image of the lean and fat phantom taken with the sandwich detector. Uncircled and circled blue arrows indicate bones and calcifications, respectively.

from a cluttered background consisting of lean and fat tissue and cancelling the contrast between them. As done for MD, the experiment was repeated for three different detector configurations by varying the intermediate copper filter, i.e., using 0-, 0.25-, and 0.5-mm thick filters. The logarithmic transmission images obtained at low and high energy while using the sandwich detector with no intermediate filter are shown in Fig. 9 as an example. As the size of the Cu filters was of approximately $10 \times 10\ \text{cm}^2$, the field of

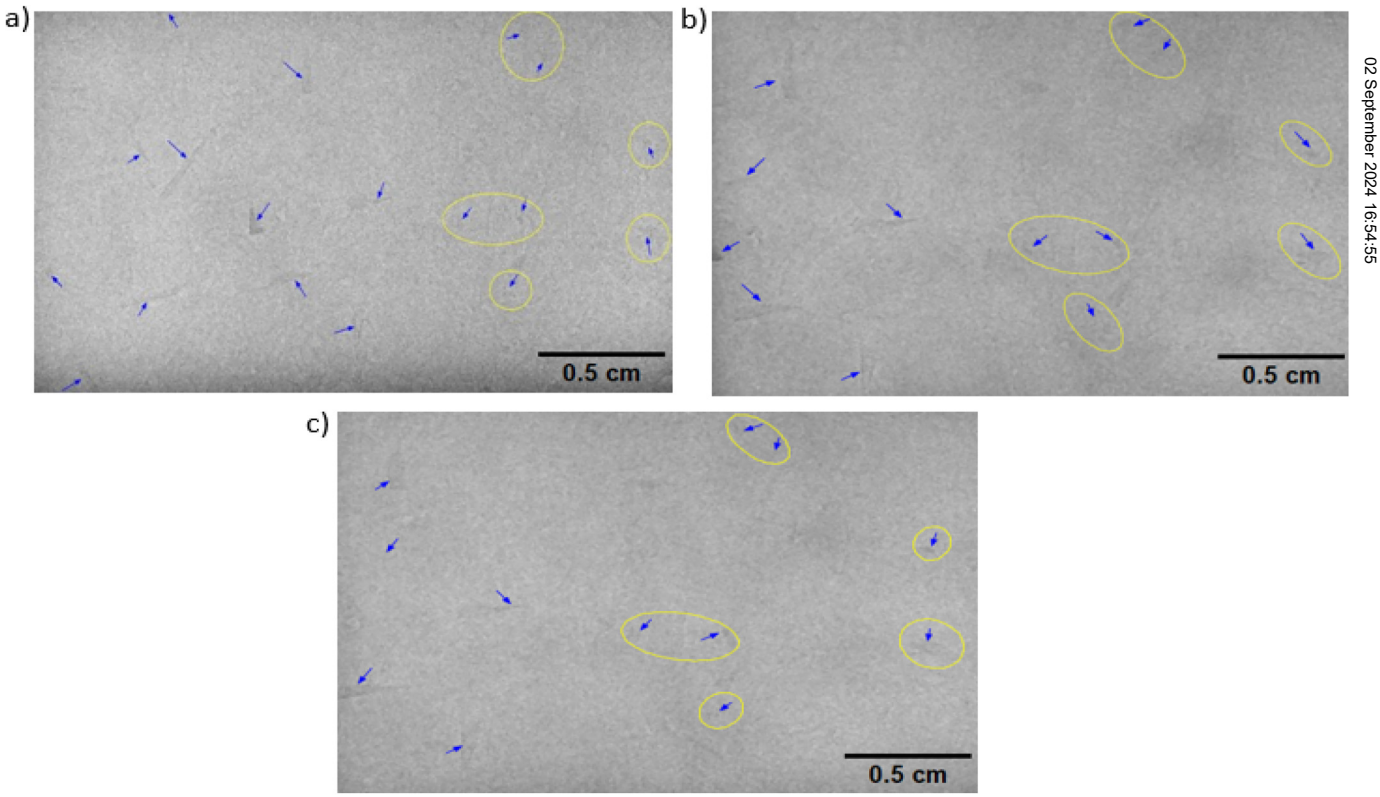

FIG. 10. Basis projection images at contrast cancellation angles for (a) no, (b) 0.25 mm (area highlighted in red in Fig. 9), and (c) 0.5 mm (area highlighted in green in Fig. 9) intermediate copper filter.

TABLE VI. SNR evaluation results at contrast cancellation angles for different intermediate filter combinations.

SNR (bone with respect to lean)					
Filter thickness (mm)	Contrast cancellation angle (ϕ)	SNR/Bone 1	SNR/Bone 2	SNR/Bone 3	SNR/Bone 4
0	45	4.8	4.3	4	4.4
0.25	44	5.9	5.5	5.8	5.5
0.5	45	3.7	2.5	3.5	3
SNR (calcium with respect to lean)					
Filter thickness (mm)	Contrast cancellation angle (ϕ)	SNR/Calc 1	SNR/Calc 2	SNR/Calc 3	SNR/Calc 4
0	45	4.7	3	3.7	2.8
0.25	44	5.8	3.9	5	5.4
0.5	45	3.8	2	2.5	2.1

view was reduced when a filter was used, and only a part of the phantom image was evaluated when using the 0.25- and 0.5-mm filters. This is shown in Fig. 9 using red (0.25 mm Cu) and green (0.5 mm Cu) dashed boxes, respectively, with the latter filter being slightly smaller. The corresponding contrast-cancelled images are shown in Fig. 10 for all three filters. In both Figs. 9 and 10, bones and calcifications are indicated with blue arrows and encircled blue arrows, respectively. The contrast basis projection images given by Eq. (15) were obtained with φ ranging from 30° to 60°, in steps of 1°, to find the angle that minimizes the contrast between lean and fat, enabling the visualization of bones and calcifications against a uniform background. The experimentally observed contrast cancellation angle is around 45°, which matches the theoretical one.

The SNR study results conducted on bones and calcifications against a lean background at the contrast cancellation angle are reported in Table VI. Four bone and calcification ROIs were selected on the projection images (as shown in Fig. 11), on which SNR evaluation was performed according to Eq. (22). The sandwich detector configuration with the 0.25 mm intermediate Cu filter showed the best SNR results; in almost all cases, the corresponding SNR values also satisfy Rose's criterion, which does not apply to the results obtained with the other two filters.

IV. DISCUSSION AND CONCLUSIONS

The study presented in this paper was aimed at designing and building an energy-integrating sandwich detector to be used for material discrimination and contrast cancellation applications. The main target was the determination of the thicknesses of the top scintillator and intermediate Cu filter, which was undertaken through a dual-energy algorithm simulation model. The model results were used to build a sandwich detector that was then tested on a range of

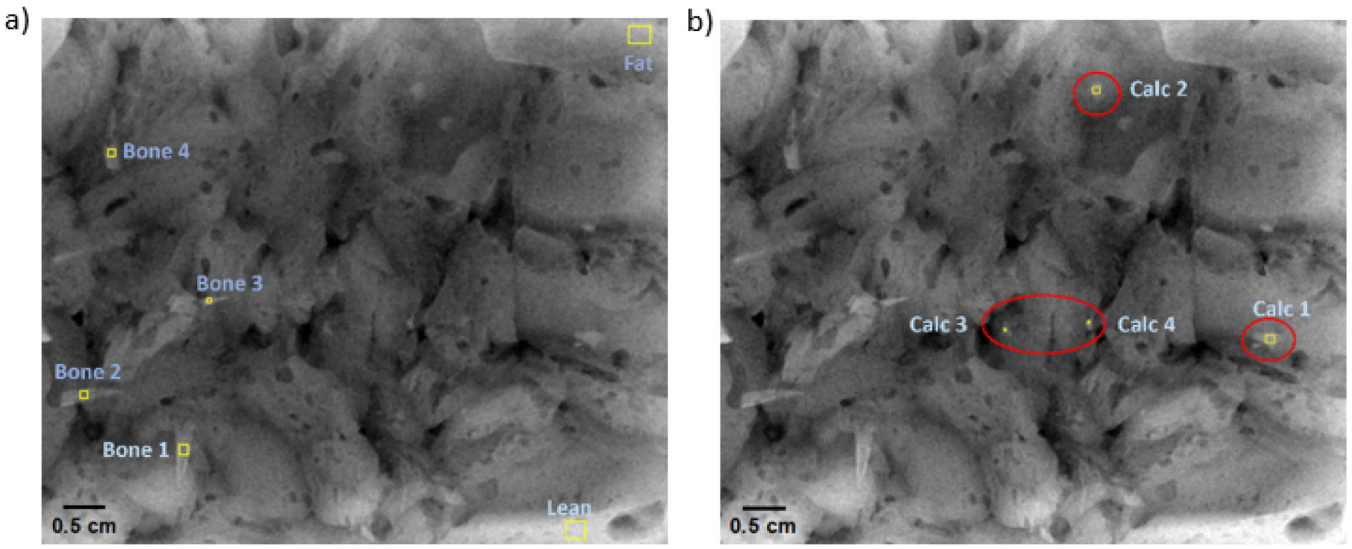

FIG. 11. Bones and calcifications ROI selection on basis projection images for SNR evaluation.

materials looking at both MD and contrast cancellation applications. All experimental studies were conducted while varying the intermediate filter thickness through 0, 0.25, and 0.5 mm of copper. All presented results indicate 0.25 mm Cu as the best choice at the considered spectral energy, which aligns with the model's prediction. This provides reassurance on the model's reliability and, therefore, also on the choice of 250 μm for the thickness of the top scintillator, which could not be verified experimentally for practical reasons.

A limitation of this study is that it deals with relatively low-Z materials imaged with relatively low x-ray energies (RQA5 beam quality). While the main reasons for this are its relatively preliminary nature and the fact that we had breast imaging and food inspection in mind as our final targets, performance at higher x-ray energies for higher Z materials should form part of future studies. The effectiveness of dual-energy methods for higher Z materials has been the subject of several studies, e.g., in the field of security inspections.[26,27] Here, they were shown to produce reliable results for Z values of up to ~22,[28,29] with higher Z being the subject of cargo inspection based on much higher photon energies produced by, e.g., linear accelerators.[30,31] On a related topic, it should also be observed that the discussed optimization is an application-specific task, which would give different results if a different x-ray spectral distribution were targeted (e.g., a thicker top scintillator, and possibly a thicker intermediate filter, for a higher kVp beam). To some extent, for similar reasons, the outcome is also influenced by the choice of the calibration materials.[32]

The developed model is simplistic and is purely based on the Beer–Lambert law; as such, it includes scattering only as a component of the linear attenuation coefficient. While some reassurance is provided by the fact that the performance of the top detector does not seem to be affected by the presence of the bottom one (and, therefore, by potential x rays backscattered by it, see below), a more thorough model would need to make use of Monte Carlo tools and take into account also scattering occurring in the sample.

Our study focuses on the use of CMOS APS sensors, but there are of course several other options that could be considered. We have mentioned state-of-the-art single photon counters,[15] which can use thresholding capabilities to perform spectral separation without the need for filters. While one of the difficulties is creating large area sensors, four-side buttable designs with increasingly small inter-module gaps are constantly being proposed,[33,34] and gaps could be virtually eliminated by means of through silicon via technologies.[35] Currently, creating a sandwich detector offers a more cost-effective solution, and indeed, important results have already been demonstrated by sandwiching amorphous silicon sensors.[10] Here, the aim was to explore the performance of a sandwich detector based on CMOS APSs; a further insight on which is provided in Figs. S5–S7 in the supplementary material, which provide modulation transfer function, sensitivity curves, noise power spectra, and detective quantum efficiencies for the bottom detector with the various choices for the intermediate Cu filter. The same metrics were extracted for the top detector, and it was observed that these are not influenced by the presence of the bottom one—as such, they are identical to those provided in Ref. 36 and are, thus, not repeated here. Comparison with the results reported in Ref. 36 for sensors with a 600 μm thick scintillator also highlights the expected loss performance of the bottom detector resulting from being exposed to a reduced x-ray flux with higher average energy. Finally, it should be noted that the development of detectors based on perovskite materials is a very active field of research,[37–39] which holds promise for the development of cost-effective and large area direct conversion devices, thereby potentially providing enhanced performance for stacked devices.

SUPPLEMENTARY MATERIAL

See the supplementary material for additional data figures omitted from the main manuscript for brevity. These include MD algorithms applied to unknown materials for scintillator thicknesses from 150 to 350 μm (Fig. S1) and for intermediate filter thicknesses of 0, 0.25, and 0.50 mm (Fig S2); the results of the χ^2 test applied to the retrieved Z_e and ρ_e values of unknown materials vs filter thickness (Fig. S3); simulated vs experimental results for unknown materials using the above filter thicknesses (Fig. S4); and finally modulation transfer function, sensitivity curve, normalized noise power spectra, and detective quantum efficiency of the bottom detector when the various filters are used, Figs. S5–S7.

ACKNOWLEDGMENTS

This study was supported by EPSRC (Nos. EP/R513143/1 and EP/T005408/1). A.O. was supported by the Royal Academy of Engineering under their Chair in Emerging Technologies scheme (No. CiET1819/2/78). J.M., A.K., Y.S., N.I., E.B., T.A., and J.B. are ISDI employees.

AUTHOR DECLARATIONS

Conflict of Interest

Yes, Jason Morehen, Asmar Khan, Yiannis Stamatis, Nicolas Iacovou, Edward Bullard, Thalis Anaxagoras, and James Brodrick are ISDI employees.

Author Contributions

Rimcy Palakkappilly Alikunju: Conceptualization (supporting); Data curation (lead); Formal analysis (lead); Investigation (lead); Methodology (equal); Software (lead); Validation (lead); Visualization (equal); Writing – original draft (lead). **Ian Buchanan:** Conceptualization (supporting); Data curation (supporting); Formal analysis (supporting); Investigation (supporting); Methodology (equal). **Michela Esposito:** Data curation (supporting); Formal analysis (supporting); Investigation (supporting); Methodology (supporting). **Jason Morehen:** Conceptualization (supporting); Investigation (supporting); Methodology (supporting). **Asmar Khan:** Conceptualization (supporting); Formal analysis (supporting); Investigation (supporting); Methodology (supporting). **Yiannis Stamatis:** Investigation (supporting); Methodology (supporting). **Nicolas Iacovou:** Investigation (supporting); Methodology (supporting). **Edward Bullard:** Conceptualization (supporting); Funding acquisition (equal); Investigation (supporting); Methodology (supporting); Project administration (supporting); Resources (equal); Supervision (supporting). **Thalis Anaxagoras:** Conceptualization (equal); Funding acquisition (equal); Investigation (supporting); Methodology (supporting); Project administration (supporting); Resources (equal);

Supervision (supporting). **James Brodrick:** Conceptualization (equal); Data curation (equal); Formal analysis (supporting); Investigation (supporting); Methodology (supporting); Project administration (supporting); Resources (supporting); Supervision (supporting); Validation (supporting); Writing – review & editing (supporting). **Alessandro Olivo:** Conceptualization (equal); Data curation (equal); Funding acquisition (equal); Investigation (equal); Methodology (equal); Project administration (lead); Resources (equal); Supervision (lead); Visualization (supporting); Writing – original draft (supporting); Writing – review & editing (lead).

DATA AVAILABILITY

The data that support the findings of this study are available from the corresponding author upon reasonable request.

REFERENCES

[1]V. Rebuffel and J. M. Dinten, "Dual-energy X-ray imaging: Benefits and limits," Insight-Non-Destr. Test. Cond. Monit. **49**(10), 589–594 (2007).

[2]R. E. Alvarez and A. Macovski, "Energy-selective reconstructions in x-ray computerised tomography," Phys. Med. Biol. **21**(5), 733 (1976).

[3]H. Watabiki, T. Takeda, S. Mitani, T. Yamazaki, M. Inoue, H. Koba, I. Miyazaki, N. Saito, S. Wada, and T. Kanai, "Development of dual-energy X-ray inspection system," Anritsu Tech. Rev. **20**, 59–66 (2013); available at https://dl.cdn-anritsu.com/ja-jp/test-measurement/reffiles/About-Anritsu/R_D/Technical/E-20/20_08.pdf

[4]Z. Ying, R. Naidu, K. Guilbert, D. Schafer, and C. R. Crawford, "Dual energy volumetric x-ray tomographic sensor for luggage screening," in *2007 IEEE Sensors Applications Symposium* (IEEE, 2007), pp. 1–6.

[5]K. Fu, *Performance Enhancement Approaches for a Dual Energy X-ray Imaging System* (University of California, San Diego, 2010).

[6]H. Martz *et al.*, "Poly- versus mono-energetic dual-spectrum non-intrusive inspection of cargo containers," IEEE Trans. Nucl. Sci. **64**(7), 1709–1718 (2017).

[7]H. E. Martz and S. M. Glenn, "Dual-energy x-ray radiography and computed tomography (No. LLNL-BOOK-753617)" (Lawrence Livermore National Lab. (LLNL), Livermore, CA, 2018).

[8]F. Fischbach, T. Freund, R. Röttgen, U. Engert, R. Felix, and J. Ricke, "Dual-energy chest radiography with a flat-panel digital detector: Revealing calcified chest abnormalities," Am. J. Roentgenol. **181**(6), 1519–1524 (2003).

[9]S. L. Maurino, K. S. Karim, V. Venkatesh, and S. Tilley, *Diagnostic Value of Single-Exposure Dual-Energy Subtraction Radiography in Lung Lesion Detection: Initial Results* (European Congress of Radiology—ECR 2022, Vienna, 2022), ECR 2022 EPOS, https://epos.myesr.org/poster/esr/ecr2022/C-15595 (accessed January 23, 2024).

[10]K. S. Karim and S. Tilley II, "Portable single-exposure dual-energy X-ray detector for improved point-of-care diagnostic imaging," Mil. Med. **188**(Supplement 6), 84–91 (2023).

[11]S. Sajja, Y. Lee, M. Eriksson, H. Nordström, A. Sahgal, M. Hashemi, J. G. Mainprize, and M. Ruschin, "Technical principles of dual-energy cone beam computed tomography and clinical applications for radiation therapy," Adv. Radiat. Oncol. **5**(1), 1–16 (2019).

[12]J. M. Lewin, P. K. Isaacs, V. Vance, and F. J. Larke, "Dual-energy contrast-enhanced digital subtraction mammography: Feasibility," Radiology **229**(1), 261–268 (2003).

[13]V. Koukou, N. Martini, C. Michail, P. Sotiropoulou, C. Fountzoula, N. Kalyvas, I. Kandarakis, G. Nikiforidis, and G. Fountos, "Dual energy method for breast imaging: A simulation study," Comput. Math. Methods Med. **2015**, 1 (2015).

[14]S. P. Osipov, V. A. Udod, and Y. Wang, "Identification of materials in X-ray inspections of objects by the dual-energy method," Russ. J. Nondestr. Test. **53**, 568–587 (2017).

[15]D. Walter, U. Zscherpel, and U. Ewert, "Recent developments of photon counting and energy discriminating detectors for radiographic imaging," in *2017 Far East NDT New Technology & Application Forum (FENDT)* (IEEE, 2017), pp. 281–285.

[16]J. Kim, D. W. Kim, S. H. Kim, S. Yun, H. Youn, H. Jeon, and H. K. Kim, "Linear modeling of single-shot dual-energy x-ray imaging using a sandwich detector," J. Instrum. **12**(01), C01029 (2017).

[17]J. Punnoose, J. Xu, A. Sisniega, W. Zbijewski, and J. H. Siewerdsen, "Technical note: Spektr 3.0—A computational tool for x-ray spectrum," Med. Phys. **43**(8), 4711–4717 (2016).

[18]See https://www.nist.gov/pml/x-ray-mass-attenuation-coefficients for X-ray mass attenuation coefficients (2022) NIST (Accessed: 12 January 2024).

[19]S. G. Azevedo, H. E. Martz, M. B. Aufderheide, W. D. Brown, K. M. Champley, J. S. Kallman, G. P. Roberson, D. Schneberk, I. M. Seetho, and J. A. Smith, "System-independent characterization of materials using dual-energy computed tomography," IEEE Trans. Nucl. Sci. **63**(1), 341–350 (2016).

[20]See https://www.isdicmos.com/company for ISDI—CMOS Image Sensor Manufacturer (accessed on December 1st, 2023).

[21]L. A. Lehmann, R. E. Alvarez, A. Macovski, W. R. Brody, N. J. Pelc, S. J. Riederer, and A. L. Hall, "Generalized image combinations in dual KVP digital radiography," Med. Phys. **8**(5), 659–667 (1981).

[22]M. Marziani, A. Taibi, A. Tuffanelli, and M. Gambaccini, "Dual-energy tissue cancellation in mammography with quasi-monochromatic x-rays," Phys. Med. Biol. **47**(2), 305–313 (2002).

[23]International Electrotechnical Commission Publication (IEC62220-1-1), Medical Electrical Equipment—Characteristics of Digital X-ray Imaging Devices—Part 1: Determination of the Detective Quantum Efficiency, IEC, 2015.

[24]A. Rose, *Vision: Human and Electronic* (Plenum, New York, 1973).

[25]D. G. Lowe, "Distinctive image features from scale-invariant keypoints," Int. J. Comput. Vision **60**(2), 91–110 (2004).

[26]K. Wells and D. A. Bradley, "A review of X-ray explosives detection techniques for checked baggage," Appl. Radiat. Isot. **70**, 1729–1746 (2012).

[27]D. Velayudhan, T. Hassan, E. Damiani, and N. Werghi, "Recent advances in baggage threat detection: A comprehensive and systematic survey," ACM Comput. Surv. **55**, 165 (2022).

[28]D. Jumanazarov, J. Koo, M. Busi, H. F. Poulsen, U. L. Olsen, and M. Iovea, "System-independent material classification through X-ray attenuation decomposition from spectral X-ray CT," NDT E Int. **116**, 102336 (2020).

[29]C.-H. Chang, Y.-C. Ni, and S.-P. Tseng, "Calculation of effective atomic numbers using a rational polynomial approximation with a dual-energy X-ray imaging system," J. X-Ray Sci. Technol. **29**, 317–330 (2021).

[30]G. Chen, G. Bennett, and D. Perticone, "Dual-energy X-ray radiography for automatic high-Z material detection," Nucl. Instrum. Methods Phys. Res. Sect. B **261**, 356–359 (2007).

[31]W. G. J. Langeveld, "Comparison of dual-energy, Z-SCAN, and Z-SPEC material separation techniques for high-energy cargo inspection," AIP Conf. Proc. **2160**, 050018 (2019).

[32]M. Magnusson, G. Alm Carlsson, M. Sandborg, A. Carlsson Tedgren, and A. Malusek, "Optimal selection of base materials for accurate dual-energy computed tomography: Comparison between the alvarez-makovski method and DIRA," Radiat. Prot. Dosim. **195**, 218–224 (2021).

[33]T. Takagi, K. Takagi, T. Terao, H. Morii, T. Okunoyama, H. Kase, A. Koike, and T. Aoki, "Photon counting X-ray imager with 4-sides buttable structure," Proc. SPIE **11693**, 1169313 (2021).

[34]V. Sriskaran, J. Alozy, R. Ballabriga, M. Campbell, P. Christodoulou, E. Heijne, A. Koukab, T. Kugathasan, X. Llopart, M. Piller, A. Pulli, J.-M. Salese, and L. Tlustos, "High-rate, high-resolution single photon X-ray imaging: Medipix 4, a large 4-side buttable pixel readout chip with high granularity and spectroscopic capabilities," J. Instrum. **19**, P02024 (2024).

[35]J. Hong, J. Grindlay, A. Branden, D. P. Violette, M. Hiromasa, D. Malta, J. Ovental, D. Bordelon, and D. Richter, "Proof of concept for through silicon vias in application-specific integrated circuits for hard x-ray imaging detectors," J. Astron. Telesc. Instrum. Syst. **7**, 026001 (2021).
[36]R. P. Alikunju, S. Kearney, R. Moss, A. Khan, Y. Stamatis, E. Bullard, T. Anaxagoras, J. Brodrick, and A. Olivo, "Effect of different scintillator choices on the X-ray imaging performance of CMOS sensors," Nucl. Instrum. Methods Phys. Res. Sect. A **1050**, 168136 (2023).
[37]Y. C. Kim, K. H. Kim, D. Y. Son, D. N. Jeong, J. Y. Seo, Y. S. Choi, I. T. Han, S. Y. Lee, and N. G. Park, "Printable organometallic perovskite enables large-area, low-dose X-ray imaging," Nature **550**, 87–91 (2017).
[38]J. Zhao, L. Zhao, Y. Deng, X. Xiao, Z. Ni, S. Xu, and J. Huang, "Perovskite-filled membranes for flexible and large-area direct-conversion X-ray detector arrays," Nat. Photonics **14**, 612–617 (2020).
[39]A. Datta, Z. Zhing, and S. Motakef, "A new generation of direct X-ray detectors for medical and synchrotron imaging applications," Sci. Rep. **10**, 20097 (2020).